Microclima: an R package for modelling meso- and microclimate

Ilya M. D. Maclean[1*], Jonathan R. Mosedale[1], Jonathan J. Bennie[2]

[1]Environment and Sustainability Institute, University of Exeter, Penryn Campus, Penryn, TR10 9FE, United Kingdom

[2]School of Geography, University of Exeter, Penryn Campus, Penryn, TR10 9FE, United Kingdom

*Corresponding author: email: i.m.d.maclean@exeter.ac.uk

Running headline: modelling meso- and microclimate

Abstract

1. Climate is of fundamental importance to the ecology and evolution of all organisms. However, studies of climate–organism interactions usually rely on climate variables interpolated from widely-spaced measurements or modelled at coarse resolution, whereas the conditions experienced by many organisms vary over scales from millimetres to metres.
2. To help bridge this mismatch in scale, we present models of the mechanistic processes that govern fine-scale variation in near-ground air temperature. The models are flexible (enabling application to a wide variety of locations and contexts), can be run using freely available data and are provided as an R package.
3. We apply a mesoclimate to the Lizard Peninsula in Cornwall to provide hourly estimates of air temperature at resolution of 100m for the period Jan-Dec 2010. A microclimate model is then applied to a one km^2 region of the Lizard Peninsula, Caerthillean Valley (49.969 ºN, 5.215 ºW), to provide hourly estimates of near-ground air temperature at resolution of one m^2 during May 2010.
4. Our models reveal substantial spatial variation in near-ground temperatures, driven principally by variation in topography and, at the microscale, by vegetation structure. At the meso-scale, hours of exposure to air temperatures at one m height in excess of 25 ºC ranged from 23 to 158 hours, despite this temperature never being recorded by the weather station within the study area during the study period. At the micro-scale, steep south-facing slopes with minimal vegetation cover experienced temperatures in excess of 40 ºC.
5. The microclima package is flexible and efficient and provides an accurate means of modelling fine-scale variation in temperature. We also provide functions that facilitate users to obtain and process a variety of freely available datasets needed to drive the model.

Key words: climate change, microclimate, microrefugia, species distributions, topoclimate, vegetation structure

Introduction

Climate is of fundamental importance to the physiology and ecology of organisms, and climatic variability has a critical influence on the behaviour, evolution and conservation of many, if not most, species (Clarke 2017). Predictive studies of climate–organism interactions usually rely on coarse-resolution climate variables derived from widely spaced point data or modelled at a resolution over tens to hundreds of kilometres. In contrast, the conditions experienced by many organisms vary over scales from millimetres to metres (Potter, Woods & Pincebourde 2013). This spatial mismatch is bridged implicitly in many models by assuming that grid-cell average climatic variables are statistically meaningful predictors of ecological responses (Bennie et al 2014). Statistical associations between organism and coarse-gridded climate data are therefore widely used, and have shown themselves be powerful predictive tools (Guisan & Thuiller 2005). However, in order to investigate mechanistic links between climate and physiology, the effects of short-term variability and the role of microclimates in buffering ecological change, fine-resolution data is required. Thus much ecological and evolutionary research is still hampered by an inability to model climate at fine-resolution (Potter, Woods & Pincebourde 2013; Suggitt et al. 2017).

Despite the tendency for ecologists to use coarse-resolution climate data, studies of microclimate have a long history and many of the processes were well understood more than 30 years ago (Geiger 1927; Hay 1979; Campbell 1986). However, many of these early studies drew on field measurements and studied aspects of microclimate at single locations. Ecologists often require data over larger spatial extents, and gridded climate data are particular useful (Hijmans et al. 2005). Recent advances in remote-sensing and the growing availability of very fine-resolution remotely-derived datasets create a timely opportunity to

present methods and models capable of generating gridded climate datasets at fine-resolution.

To date, several approaches to downscaling from coarse-gridded to fine-scale microclimate data have been used by ecologists. Dynamical downscaling, through the use of regional climate models that apply the full physics of global climate models at a fine-scale (Murphy 2000), have the advantage that they can generate internally consistent data for variables and represent synoptic systems. However, due to high computing requirements they are rarely a practical solution for producing data at resolutions below five km. Physically-based boundary-layer models of atmospheric processes at finer scales (for example down to one m resolution) are usually limited in application to a small extent and highly simplified landscapes. Land surface models (for example JULES, the UK land surface simulator) apply physical equations to solve the energy and water balance at a point, or across a grid, and in doing so predict key ecological variables such as near-surface temperature and humidity. However, while land surface models incorporate vertical processes such as radiative heating of the surface and canopy shading, they do not incorporate meso-scale processes such as variation in wind speed, elevational lapse rates or lake/ocean effects. While land surface models have been adapted for use in an ecological context (Bennie et al. 2010), most physically-based models are primarily designed for meteorological or hydrological applications. A notable exception is the NicheMapR package in R (Kearney & Porter 2017), which is explicitly designed to mechanistically model the energy and mass budgets of organisms and their microclimate (including soil and snow), and has been widely tested (see e.g. Kearney et al. 2014). Finally, GIS-based statistical downscaling techniques apply empirical corrections (usually based on slope, aspect and elevation) to map climatic variables, and have been used in several studies to produce fine-resolution maps for species distribution modelling (e.g. Milling et al. 2018).

The models and R package described here are not intended to replace physically-based regional climate models, land surface schemes or mechanistic approaches to the energy

budget of organisms and their environment such as NicheMapR. Of note, however, many of required to model near-ground temperature are similar to those required for modelling the heat budget organisms, and the functions in microclima may be of use in so doing. However, our primary intention is to bridge the gap between the landscape and local-scale processes that cause spatial variation in temperature and can be modelled using fine-resolution Digital Terrain Models (DTMs) and point-based models to determine the energy balance (Table 1). We develop a flexible hybrid physically- and empirically- based approach in which the spatial patterns of physical factors directly influencing the near-ground temperatures at a point are calculated, and the relative influence of these factors within a given landscape or region can be fitted to data by empirically-derived parameters. This hybrid approach to mapping climatic variables at a fine scale is suitable for many ecological applications, avoiding the complexity and computational costs of attempting to fully resolve the physics of atmospheric processes at high resolution, but retaining much of the generality of a physically-based model. The models are designed to be flexible, enabling application in a wide variety of circumstances, though their modular design is such that easy development of improvements for application in specific circumstances is also possible. The models can also be easily applied using freely available data. While computing constraints remain a challenge, the models could, in theory, be applied over large spatial extents. The R package can be installed from https://github.com/ilyamaclean/microclima. The help documentation associated with the R package is included here (Appendix S3 and 4).

Materials and methods

Two nested models are presented: a mesoclimate model for estimating local variation in ambient air temperature and a microclimate model for estimating finer-scale variation in near-ground temperatures. The microclimate model derives very fine-resolution (<5m) near-surface temperatures from weather station data or from the outputs of the mesoclimate model. The model is applied over one km^2 of coastal Cornwall (Caerthillean Valley, 49.971 ºN, 5.214 ºW; Fig 1a) to provide hourly temperature estimates for May 2010. The mesoclimate model derives

moderate fine-resolution (~100m) air temperatures at one m above the ground from coarse-gridded climate data. The model is applied to the Lizard Peninsula in Cornwall (50.0 ºN, 5.2 ºW; Fig 1b) to provide hourly temperature estimates for the whole of 2010.

Microclimate model

Temperature

From Bennie et al (2008), the difference between near-surface temperature (T_0) and reference air temperature (T), i.e. that derived from a weather station or the mesoclimate model, is given by:

$$T_0 - T = \frac{r_{HR}}{\rho c_p}\left(R_{net} - L - G\right) \quad (1)$$

where R_{net} is the net radiation flux, L is the latent heat flux, G is the heat flux into the soil, ρ is the density of air, c_p is the specific heat of air at constant pressure and r_{HR} is a resistance for the loss of sensible heat. For efficient modelling of hourly surface temperature it is assumed that the most important energy fluxes determining near-surface temperature are those due to radiation and sensible heat flux that occur at the surface–atmosphere boundary. Heat fluxes into the soil and latent heat exchange are considered to be small and proportional to net radiation, and the heat capacity of the vegetation is considered to be relatively small so that, compared to the hourly time scale of the model, surface temperatures rapidly reach equilibrium. The difference between the near-ground temperature and the ambient temperature is thus a linear function of R_{net}, the gradient of which is a measure of the thermal coupling of the surface to the atmosphere. If this relationship is applied to vegetation, assuming the canopy to act like a surface, while both ρ and c_p are constant, r_{HR} varies as a function of both the structure of the vegetation and wind speed and can be fitted to field calibration data using function `microfit` (see also equation 7).

Radiation

The net radiation flux is determined by the balance of incoming shortwave radiation and emitted longwave radiation, with the former portioned between direct (R_{dir}) and diffuse (R_{dif}) components. Shortwave radiation is modified by topography and vegetation cover and downscaled using function `shortwaveveg`. Topography determines whether a given location is shaded and also the angle at which the sunlight strikes the surface. Vegetation attenuates radiation as it passes though the canopy.

From Bennie et al. (2008), the direct radiation flux on an inclined surface is given by:

$$R_{dir} = R_{beam}(\cos Z \cos S + \sin Z \sin S \cos(\Omega_s - \Omega)) \quad \text{if } A \geq H$$

$$R_{dir} = 0 \quad \text{if } A < H$$

where R_{beam} is the direct beam radiation flux on a surface perpendicular to the beam, Z is the solar zenith, S is the angle of the slope of the surface, Ω_S is the solar azimuth, Ω is the slope aspect, A is the solar altitude and H is the local horizon angle in the direction of the sun. Z, A and Ω_S can be readily determined for a given time and geographic position and the slope and aspect of a surface and local horizon angles from digital elevation data.

From Hay & McKay (1985), the diffuse radiation flux can be partitioned into that which is isotropically distributed (R^*_{dif}), that which exhibits anistropic properties (R'_{dif}) and that which is reflected back from surrounding surfaces (R^S_{dif}):

$$R^*_{dif} = 0.5sR_{dif}(1 + \cos S)(1 - k)$$

$$R'_{dif} = R_{dif}k(\cos Z \cos S + \sin Z \sin S \cos(\Omega_s - \Omega)) \quad \text{if } A \geq H$$

$$R'_{dif} = 0 \quad \text{if } A < H$$

$$R^S_{dif} = 0.5R_{dif}\alpha_S\left(1 - \cos\left(S + S^*\right)\right)$$

where α_S is the mean albedo of the surrounding surface and S^* is the mean slope of the adjacent surfaces. The relative partitioning of radiation depends on an "anisotropy index" (k) given by:

$$k = \frac{R_{beam}}{R_0}$$

where R_0 is the extraterrestrial radiation flux (~4.87 MJ m^{-2} h^{-1}) and s is a correction for the proportion of sky, calculated using function `skyviewtopo`, as follows:

$$s = 0.5\cos(2\overline{H}) + 0.5 \quad (2)$$

where $\overline{H}$ is the mean horizon angle.

The transmission of radiation by vegetation is described using an equation similar to Beer's Law (Campbell 1986):

$$R_{veg} = (1 - a_g)\left[\left(R_{dir} + R'_{dif}\right)\exp(-K'L_{AI}) + \left(R^*_{dif} + R^S_{dif}\right)\exp(-K^*L_{AI})s_{veg}\right]$$

where R_{veg} is the flux density of radiation absorbed by the ground below leaf area index (L_{AI}), α_g is the albedo of the ground below the canopy, K' and K^* are the isotropic and anisotropic coefficients of the canopy and s_{veg} is an adjustment applied if the sky view above the canopy is partially obscured (see later). K' is a function of solar inclination and leaf distribution character of the canopy. From Campbell (1986), a broad range of leaf types can be represented by an ellipsoidal distribution, and the extinction coefficient can thus be expressed as follows:

$$K' = \frac{\sqrt{x^2 + 1/\tan^2 A}}{x + 1.774(x + 1.182)^{-0.733}} \quad (3)$$

Here x is determined by canopy architecture and is the ratio of vertical to horizontal projections of a representative volume of foliage, and in our model is estimated allometrically from vegetation height using function `leaf_geometry` (Appendix S2). The extinction coefficient for isotropic component of radiation (K^*) can be obtained by integrating over the portion of the hemisphere in view. For computational efficiency, the integral can be closely approximated by equation 3, with A (in degrees) substituted by a parameter A* which, for a given values of x, can be derived from L_{AI} as follows:

$$A^* = p_1 L_{AI}^{1/3} + p_2$$

where p_1 and p_2 are coefficients unique to each x (Table S3). If the sky view above the canopy is partially obscured, then the integral is between the limits determined by $\overline{H}$ and the sky view correction factor (s_{veg}) is applied. In function `skyviewveg`, this integral is approximated by equation 2, with $\overline{H}$ replaced by H^*:

$$H^* = 90\frac{H^c}{90^c}, \text{ where: } c = p_3 L_{AI}^{p_4} + 0.564 \quad (4)$$

Here, p_3 and p_4 are parameters unique to each value of x (Table S4).

Following Konzelmann et al. (1994), and assuming that differences in R_{lw} caused by difference between T and T_0 are small, the net flux of longwave radiation under vegetated canopies (R_{lw}), calculated using function `longwaveveg`, can be approximated as follows:

$$R_{lw} = s_{veg}\left(\sigma T^4 - R_{lwg} + R_{lwe} + R_{lwc}\right)$$

where σ is the Stefan-Boltzmann constant (2.043 x 10^{-10} MJ m^{-2} $hour^{-1}$), R_{lwg} is radiation emitted back from the atmospheric that passes through gaps the canopy, R_{lwe} is radiation scattered downwards from leaves, R_{lwc} is radiation emitted by the canopy and T is temperature in Kelvin.

The flux of radiation that passes through gaps in the canopy is given by:

$$R_{lwg} = \exp(-K^* L_{AI}) R_{lsky}$$

R_{lsky} is radiation scattered back from the atmosphere which, assuming that differences in R_{lw} caused by differences between T and T_0 are small, can be calculated as follows:

$$R_{lsky} = \varepsilon \sigma T^4$$

Here ε is the emissivity of the atmosphere, which can be determined as follows (Klok & Oerlemans 2002):

$$\varepsilon = \left(0.23 + 0.433 \left(\frac{e_a}{T}\right)^{1/8}\right)(1 - n^2) + 0.976 n^2$$

where n is fractional cloud cover and e_a is vapour pressure in kPa.

From Zhao & Qualls (2006) the flux of radiation scattered downward through leaf reflection is given by:

$$R_{lwl} = (1 - \alpha_c)(1 - r)[1 - \exp(-K^* L_{AI})] R_{lsky}$$

where α_C is the albedo of the canopy and r is the fraction of downward radiation scattered upwards, estimated as:

$$\log_e\left(\frac{r}{1-r}\right) = \frac{2}{3}\log_e(x+1)$$

R_{lwc} is given by:

$$R_{lwc} = 0.51(1-\alpha_c)[1-\exp(-K^* L_{AI})]\sigma T^4$$

Wind speed

Wind speeds are affected by local terrain, and to account for this, function `windheight` implements the logarithmic wind-height profile assumed by Allen et al. (1998), and function `windcoef` applies the shelter coefficient described by Ryan (1977), as follows:

$$u_1 = 0.635 u_{10}\left(1-\frac{\arctan(0.17 H_w)}{1.65}\right) \quad (5)$$

where u_1 is local wind speed at one m above the ground, u_{10} is the wind speed at 10 m height and H_w is the tangent of the horizon angle upwind at one m above the ground.

Mesoclimate model

The mesoclimate model provides estimates of air temperature and ignores the effects of radiation transmissions though canopies and variation in ground surface albedo, as these are accounted for in the microclimate model. Differences between local temperatures (T_1) and reference air temperature (T) are derived as a function of coastal, cold air drainage and elevation effects and also the effects of meso-scale topography on the radiation flux, as in equation 1:

$$T_1 - T - \Delta T_E - \Delta T_C - \Delta T_K = \frac{r_{HR}}{\rho c_p}(R_{net} - L - G)$$

here ΔT_E is the difference in temperature due to elevation, ΔT_C is the difference in temperature due to coastal effects and ΔT_K is the difference in temperature due to cold-air drainage.

Elevation

Differences in temperature due to elevation are calculated as follows:

$$\Delta T_E = \Delta z \Gamma_w$$

where Δz is the difference in elevation (m) between the locations of T and T_1 and Γ_m is the lapse rate, calculated using function `lapserate`, as follows (Hess 1959):

$$\Gamma_m = g\left(1 + \frac{L_v r_v}{QT}\right)\left(c_{pd} + \frac{0.622 {L_v}^2 r_v}{QT^2}\right)^{-1}$$

where g is gravitational acceleration (9.8076 ms^{-1}), L_v is the latent heat of vaporisation (2,501,000 Jkg^{-1}), Q is the gas constant for dry air (287 $Jkg^{-1}K^{-1}$), c_{pd} is the specific heat of dry air at constant pressure (1003.5 $Jkg^{-1}K^{-1}$), T is the reference temperature and r_v is the mixing ratio of water vapour given by:

$$r_v = \frac{0.622 e_a}{P - e_a}$$

where P is atmospheric pressure (Pa).

Coastal effects

Coastal effects are derived using function `coastalTps`, which uses thin-plate spline interpolation with three covariates to derive finer resolution temperature estimates for each time step from coarse-gridded reference temperature data. The three covariates are: differences between sea and reference land temperature, coastal exposure in an upwind direction and coastal exposure irrespective of direction. Upwind exposure is calculated as the inverse-distance^2 weighted proportion of sea upwind of each location and general exposure by numerically integrating this ratio at fixed intervals over the full 360º.

Cold-air drainage

ΔT_K is modelled as follows:

$$\Delta T_K = -I_C \Gamma_m \Delta z_m \log F \quad (6)$$

where I_C is a binary variable, conditional on time of day, wind speed and emissivity, as cold air drainage typically occurs at night or shortly after, and in calm, still conditions (Barr & Orgill 1989). The function `cadconditions`, used for calculating I_C allows the user to specify these conditions. Δz_m is the elevation difference in metres of a given location and the highest point of a drainage basin, and F is accumulated flow expressed as a proportion of the maximum in each basin, and calculated using function `flowacc`. Quantification of F and Δz_m requires drainage basins to be delineated, using function `basindelin`.

Data

To calibrate and run the models, the following high spatial, low temporal resolution datasets are needed (summarised in Appendix S5). (1) Digital elevation data. Such data are widely available at very fine-resolution for specific regions of the world, or globally at 30m from the Shuttle Radar Topographic Mission (Farr et al. 2007). (2) Estimates of leaf area and albedo.

Both measures can be readily derived from multi-spectral aerial or satellite imagery. (3) Estimates of the leaf distribution character of vegetation. This can be approximated using airborne LiDAR data (Appendix S2) or potentially by performing image classification to identify specific vegetation types. In addition, the following high temporal, low spatial resolution datasets are needed. (1) Surface pressure, wind speed and direction, humidity and temperature. These variables are routinely recorded by weather stations and also available as global datasets (e.g. Kalnay et al.1996). (2) Direct and diffuse radiation and cloud cover. These datasets are freely available for most of the globe (Posselt et al. 2012). Additionally sea-surface temperature data are required, though coarse spatial and temporal data are adequate (see e.g. Rayner et al. 1996 for a global dataset). We used the following datasets.

Digital Elevation Data. A Digital Surface Model (DSM), representing the elevation of the top of vegetated surfaces, and a DTM, representing the elevation of the underlying ground were obtained from the Tellus SW Project (CEH, Wallingford). Both are provided at a grid resolution of one m. We used the DTM layer for calculating slope, aspect and topographic shading and the DSM layer for calculating wind shelter, and both to calculate vegetation height. For the mesoclimate model, data were coarsened by computing mean values within each 100 m grid cell.

Vegetation characteristics. Following e.g. Carlson & Ripley (1997), we estimated leaf-area index from the normalized difference vegetation index (NDVI), using visual and colour-infrared aerial imagery obtained from Bluesky International Ltd (Coalville, UK; imagery captured 11th Sep 2009; Fig. S4a). We estimated the leaf distribution character of vegetation from vegetation height (Appendix S2 and function `lai`).

Albedo. We derived albedo from the same visual and colour-infrared aerial imagery, adjusting values for brightness and contrast using MODIS data obtained from USGS Land Processes Distributed Archive Centre (Appendix S2 and functions `albedo` and `albedo_adjust`).

366

367 *Cloud cover and shortwave radiation.* We used 0.05º gridded satellite-derived estimates of
368 cloud cover, and direct and diffuse radiation (Posselt et al. 2012). Radiation data are available
369 hourly, though missing values and those within an hour either side of sunrise and sunset, for
370 which satellite estimates are unreliable (Posselt et al. 2012), were imputed (Appendix S2).
371 Cloud cover is available at ~15 minute intervals and each grid cell is assigned a value of 'full',
372 'partial' or 'unobscured'. Fractional cloud cover was calculated by calculating the mean in each
373 hour, making the assumption that partial cloud cover equates to fractional value of 0.5.

374

375 *Surface pressure and wind data*. We obtained six-hourly surface pressure and wind data from
376 the National Center for Environmental Prediction (Kalnay et al. 1996). These data are available
377 at a grid cell resolution of 2.5º, and the values for the grid cell corresponding to our study area
378 were extracted. Values were then interpolated to hourly data using a cubic-spline.

379

380 *Humidity and temperature.* Daily specific humidity data, mean daily near-surface air
381 temperature, and daily temperature ranges, available at a one km grid resolution, were
382 obtained from the Centre for Ecology and Hydrology Climate (Robinson et al. 2015). Hourly
383 specific humidity data were derived by interpolation using a cubic-spline. To derive hourly
384 temperature data, we implemented a more complex interpolation algorithm, whereby diurnal
385 patterns and variation in cloud cover and radiation are accounted for (Appendix S2 and
386 function `hourlytemp`).

387

388 *Sea-surface temperature*. We obtained one degree gridded datasets of monthly sea ice and
389 sea surface temperatures, available as a global dataset from the Met Office Hadley Centre
390 (Rayner et al. 1996), and extracted data for the grid cell corresponding to our study area. We
391 obtained hourly values using cubic-spline interpolation, assuming that the mean value for each
392 month corresponded to the mid-point of that month. Due to the high volume and specific heat

capacity of water, sea surface temperatures undergo only minor high frequency fluctuations, so simple interpolation was deemed reasonable.

Model fitting

Prior to fitting the mesoclimate model we accounted for cold-air drainage, elevation and coastal effects. To calculate elevation effects, we first removed the fixed lapse-rate applied to the temperature data and then applied our variable one.

To fit our mesoclimate model, 56 iButton thermachrons were deployed across the Lizard Peninsula between 1st March and 31st Dec 2010, and set to record temperatures at hourly intervals. Loggers were placed to capture the full spatial gradients in the main determinants of climate in order to minimise extrapolation errors, and provided 137,218 measurements of temperature. Loggers were attached to a wooden pole one m above the ground. To fit the microclimate model, 55 iButton thermachrons were deployed in Caerthillean Valley on the Lizard Peninsula (49.9687 ºS, 5.2142 ºW), from 10th-31st May 2010. Loggers were set to record temperatures at 10 minute intervals, and the mean temperature in each hour used to calibrate the model. 27,530 hourly temperature measurements were obtained. The valley is a coastal grassland with complex topography, enabling temperatures to be recorded across a wide range of slopes and aspects and in vegetation of varying height. Loggers were attached to a short wooden stake 5 cm above the ground. In both instances, loggers were orientated north, and shielded from direct sunlight using a white plastic screen. Data from half the loggers was used for calibration and from the rest for testing.

Temperature anomalies ($T_0 - T$) were modelled using standard linear regression as a function of the following sets of terms:

$$T_0 - T = \beta_1 + \beta_1 R_{net} + \beta_1 u_f + \beta_1 R_{net} u_f + \beta_1 \Delta T_K + \varepsilon_i \quad (7)$$

Here u_f is a factor that allows the relationship with net radiation to vary with wind speed, set at 0 when wind speeds at one m are below 3.66 ms^{-1}, and one when above (β_4 is assumed to be negative), with this threshold established by iteratively trying out different thresholds, and selecting that which yielded the best fit. The terms $\beta_{1...5}$ are coefficients estimated by linear regression and ε the error associated with each term *i*. Other terms have already been defined. The terms are listed in anticipated descending order of importance. We first assessed whether including each set of terms improved model performance by computing the Akaike Information Criterion (AIC) and then estimated coefficients associated with each term using standard linear regression. To reduce the effects of temporal autocorrelation we randomly selected 2000 of the temperature measurements and repeated the analyses 9999 times, computing AICs and coefficient estimates for each model run. Median model coefficient estimates were then used to drive our model. The microclimate model was fitted in the same way, except that here (T_0 – T) is the difference in near ground temperatures at the output of the mesoclimate model and the value of u_f that yielded the best fit was 0.398 ms^{-1}. The function `fitmicro` implements the method described above, though also includes the option to use all data for fitting.

Running and testing the model

Both models can be run using function `runmicro` and fully executable examples are provided in the associated help file. We ran the models in hourly time steps for the period 1st January to 31st December 2010 (mesoclimate model) and 1st – 31st May 2010 (microclimate model), deriving temperature estimates for each grid cell of our study areas. The model was then tested by comparing model predictions with the observed data obtained from 56 loggers placed at separate locations within the study site over the same period. The model was relatively computationally efficient. On a standard desktop, the model fitting procedure took 29 seconds. The time taken to run the model on a 1000 x 1000 pixel dataset took 0.25 seconds for one time-step, equating to just 36 minutes for a year (though additional time is required to write model outputs to disk).

Results

In all 9999 model simulations both sets of models performed best when all terms were included. This mesoclimate model explained 90.8% of the variation in local temperature anomalies and 96.2% of the variation in total temperature, with a Mean Absolute Error (MAE) of 0.97 ºC and Root Mean Square Error (RMSE) of 1.23 ºC (Figs. 2a,c). The microclimate model explained 78.7% of the variation in local temperature anomalies and 90.9% of the variation in total temperature, with a MAE of 1.25 ºC and RMSE of 1.61 ºC (Figs. 2a,c). Model coefficients for both the meso- and microclimate model are shown in Table 2.

At the meso-scale, there was relatively little spatial variation in mean temperature, which in 2010 ranged from 8.6 to 10.0 ºC (Fig. 3a). The warmest temperatures were in sheltered low-lying coastal valleys, particularly on south-facing slopes. Minimum temperatures ranged from -6.7 to -5.3 ºC, being coldest at higher elevations and inland (Fig. 3b). Maximum temperatures ranged from 27.2 to 31.2 ºC, and were highest on low-lying south-facing slopes (Fig. 3c). There were larger differences in bioclimate variables. Accumulated-degree hours varied from 8,446 to 16,008 (Fig. 3d), hours of exposure to temperatures below 0 ºC from 391 to 669 (Fig. 3e), and hours of exposure to temperatures in excess of 25 ºC from 23 to 158 (Fig. 3f).

At the micro-scale, there was greater temperature variation, with mean temperatures in May 2010 varying from 12.0 to 16.7 ºC (Fig. 4a). The warmest temperatures were on south-facing slopes with short vegetation. Minimum temperatures ranged from 3.4 to 5.7 ºC and were primarily affected by vegetation cover, being coldest in sparsely vegetated areas with a clear horizon (Fig. 4b). Maximum temperatures varied from 25.2 to 41.8 ºC, with the highest temperatures recorded on dark, sparsely-vegetated, south-facing rock faces (Fig. 4c). There were also large differences in bioclimate variables. Growing-degree hours varied from 1,644 to 4,223 (Fig. 4d), mean diurnal temperature variation from 11.1 to 21.3 ºC (Fig. 4e) and hours of exposure to temperatures in excess of 30 ºC from 0 to 53 (Fig. 54).

Discussion

The main aim of this study is to present general methods for modelling micro- and mesoclimate that can be readily applied to determine the range in near-ground air temperatures experienced by organisms across any landscape or region. While the models accurately predict temperatures at locations other than those used for model calibration, their transferability to different sites altogether has yet to be tested and, although calibration and testing were performed under a wide range of climatic conditions, there may be errors associated with extrapolating the model beyond the conditions used for calibration. However, an important characteristic of our models is that the spatial patterns of variables are based on the underlying physics of heat budgets and airflow rather than on spatial interpolation, and while recalibration or the incorporation of other macro- to micro-scale processes may be necessary at some locations, the physical laws governing these processes are universal.

Overall, the predictive power of our models compare well with other more location-specific models (Pike, Pepin & Schaefer 2013; Aalto et al., 2017), and build on previous methods by presenting a method for capturing the effects of vegetation structure on microclimate (cf. Bennie et al 2008) or by incorporating mesoclimatic processes (cf. Kearney et al. 2017). Nonetheless, some aspects of the model remain poorly developed, in part due to the limited extent over which it has been tested, and hence, the range of conditions that influence climatic processes within our study area. Key among these is the effects of latent heat flux on temperatures, which can be particularly important in cold environments, where snow freeze-thaw is frequent (Weller & Holmgren 1974), or under drought conditions when soil temperatures may heat up by more than predicted (Hunt et al. 2002). In contrast to other models (e.g. Kearney et al. 2017), heat exchange between the soil and near-ground air layer and heat storage in the soil are also unaccounted for, and may result in delayed effects of radiation on near-ground temperatures. Environmental lapse-rates are also rather crudely handled by our model; for our study area this does not cause large errors due to the limited elevation range, but further development and testing may be necessary for applications in

505 mountainous regions. A further limitation is that our model does not presently account for
506 seasonal variation in albedo, which in temperate regions can be significant due to leaf-loss in
507 winter, and in Arctic regions may be influenced strongly by snow cover (Weller & Holmgren
508 1974; Aalto et al. 2017). Vegetation structure is also rather simplistically determined from
509 aerial imagery. Better three-dimensional assessment of seasonal variation in vegetation
510 structure, made possible through full-waveform laser-scanning for example (Wagner et al.
511 2008), represents one of the best opportunities for further development. These limitations
512 aside, our models provide accurate physically based predictions of the effects of topography
513 and vegetation on local scale climate at the landscape scale.
514
515 At both micro- and meso-scales, slope and aspect are the principal determinants of spatial
516 variation in maximum temperatures, with the warmest temperatures on steep south-facing
517 slopes. However, at the micro-scale, where surface albedo and vegetation structure are also
518 accounted for, these also exert a strong influence, with temperatures highest on dark surfaces
519 with sparse vegetation cover. This is to be expected given the overriding importance of net
520 solar radiation on temperature (Geiger 1927). At the meso-scale, elevation and coastal effects
521 dominate spatial variation in minimum temperatures, though variation is small, reflecting the
522 limited elevational range and maritime nature of our study area. At the micro-scale, vegetation
523 cover exerts the greatest influence on minimum temperature, though the degree of
524 topographic sheltering has opposing influences, decreasing temperatures due to low wind
525 speeds, but increasing them by influencing the degree of longwave radiation that is reflected
526 from adjacent surfaces. During May, the coldest temperatures were recorded on a calm night
527 in relatively exposed areas with short vegetation, where temperatures were up to two ºC cooler
528 than in vegetated areas. Dense vegetation thus serves to buffer microclimates, with mean
529 daily temperature ranges approximately 10 ºC greater in sparsely vegetated areas than in
530 areas with dense vegetation.
531

532 Longer-term temperature records from Culdrose weather station on the Lizard Peninsula
533 reveal that 2010 was a particularly cold year, with mean annual temperatures approximately
534 0.8 ºC cooler than the 1977-2016 baseline (Maclean et al. 2017). This is largely due to the
535 particularly cold winter that affected much of north and north-western Europe, caused by
536 record persistence of the negative phase of the North-Atlantic Oscillation (Cattiaux et al. 2010).
537 The total number of frost-hours (<0 ºC) recorded at Culdrose was the greatest on record, more
538 than eight times higher than the 1977-2016 median. This is reflected in spatial patterns of frost
539 exposure across the study region, which even in sheltered valleys is relatively high, despite
540 being frost frost-free in many years (Maclean et al. 2017). Rather uncharacteristically, the
541 maximum recorded temperature in 2010, 22.3 ºC, was recorded at 16:00 hours on the 25th of
542 May, whereas in most other years maximum temperatures are recorded in July (Maclean et
543 al. 2017). The range in maximum temperatures predicted across the study area relative to that
544 recorded at the weather station serves to illustrate an important point: maximum temperatures
545 at or close to the ground are almost universally much warmer than those recorded by weather
546 stations inside a Stevenson Screen. At the meso-scale, hours of exposure to temperatures in
547 excess of 25º C ranged from 23 to 158 hours, despite this temperature never being recorded
548 by the weather station within the study area. At the micro-scale, all areas except sheltered
549 gullies in cliffs experienced some exposure to temperatures in excess of 30 ºC, and maximum
550 temperatures on steep south-facing cliffs with little vegetation cover exceeded 40 ºC. In
551 contrast, minimum temperatures were only marginally cooler than those recorded at the
552 weather station (-5.9 ºC in 2010, 3.6 ºC in May 2010).
553
554 Biological responses to climate change within our study region are influenced strongly by fine-
555 scale spatial and temporal variation (Maclean et al. 2015). Consequently, predictions of the
556 responses of species to climate change will need to account for the spatial variation in
557 microclimate at resolution smaller than most available climate data, and the dynamics of
558 microclimate at a temporal resolution smaller than long-term climatic means. More generally,
559 the study of relationships between species and climate is currently hampered by the coarse

560 resolution at which climate is currently modelled (Potter, Woods & Pincebourde 2013; Bramer
561 et al 2018; Suggitt et al. 2018). This study is intended to demonstrate the importance of fine-
562 scale variation in temperature and to show that this variation can be modelled.
563
564 **Acknowledgments**
565 We thank Michael Kearney and two anonymous referees for useful comments on the
566 manuscript, Phillipa Gillingham, Robin Curtis and Isobel Bramer for help with fieldwork and
567 Robert Wilson for conceptual advice. We also thank Katie Thurston for proof-reading, though
568 any remaining mistakes are the authors' responsibility. This research was part-funded by the
569 European Social Fund Project 09099NCO5 and NERC NE/P016790/1.
570
571 **Authors' contributions**
572 IMDM conceived and coded the model, obtained the majority of data, performed analyses and
573 wrote the manuscript. JM assisted with coding the functions associated with cold-air drainage
574 and commented on the manuscript. JB assisted with coding the functions associated with
575 downscaling radiation, helped with placement of temperature loggers and edited the
576 manuscript.
577
578 **Data accessibility**
579 The data used in this study are included with the R package, available at
580 http://doi.org/10.5281/zenodo.1411517.
581
582 **References**
583 Aalto, J., Riihimäki, H., Meineri, E., Hylander, K. & Luoto, M. (2017) Revealing topoclimatic
584 heterogeneity using meteorological station data. *International Journal of Climatology*,
585 37, 544-556.

586 Allen, R.G., Pereira, L.S., Raes, D. & Smith, M. (1998) Crop evapotranspiration-Guidelines for
587 computing crop water requirements. *FAO Irrigation and Drainage Paper 56*. FAO,
588 Rome.
589 Barr, S. & Orgill, M.M. (1989) Influence of external meteorology on nocturnal valley drainage
590 winds. *Journal of Applied Meteorology,* 28, 497-517.
591 Bennie, J., Huntley, B., Wiltshire, A., Hill, M.O. & Baxter, R. (2008) Slope, aspect and climate:
592 spatially explicit and implicit models of topographic microclimate in chalk grassland.
593 *Ecological Modelling,* 216, 47-59.
594 Bennie, J., Wilson, R.J., Maclean, I.M.D. & Suggitt, A.J. (2014) Seeing the woods for the trees-
595 when is microclimate important in species distribution models? *Global Change Biology*,
596 20, 2699-2700.
597 Bennie, J., Wiltshire, A.J., Joyce, A.N., Clark, D., Lloyd, A.R., Adamson, J., Parr, T., Baxter,
598 R. & Huntley, B. (2010). Characterising inter-annual variation in the spatial pattern of
599 thermal microclimate in a UK upland using a combined empirical–physical model.
600 *Agricultural and Forest Meteorology*, 150, 12-19.
601 Bramer, I., Anderson, B.J., Bennie, J., Bladon, A.J., De Frenne, P., Hemming, D., Hill, R.,
602 Kearney, M.R., Körner, C., Korstjens, A.H. et al. (2018) Advances in monitoring and
603 modelling climate at ecologically relevant scales. *Advances in Ecological Research*,
604 58, 101-161.
605 Campbell, G. (1986) Extinction coefficients for radiation in plant canopies calculated using an
606 ellipsoidal inclination angle distribution. *Agricultural and Forest Meteorology,* 36, 317-
607 321.
608 Carlson, T.N. & Ripley, D.A. (1997) On the relation between NDVI, fractional vegetation cover,
609 and leaf area index. *Remote Sensing of Environment,* 62, 241-252.
610 Cattiaux, J., Vautard, R., Cassou, C., Yiou, P., Masson-Delmotte, V. & Codron, F. (2010)
611 Winter 2010 in Europe: a cold extreme in a warming climate. *Geophysical Research*
612 *Letters,* 37, L20704.

613 Clarke, A.J. (2017) *Principles of Thermal Ecology: Temperature, Energy and Life*. Oxford
614 University Press, Oxford.
615 Farr T.G., Rosen, P.A., Caro, E., Crippen, R., Duren, R., Hensley, S., Kobrick, M., Paller, M.,
616 Rodriguez, E., Roth, L. et al. (2007) The shuttle radar topography mission. Reviews
617 of Geophysics, 45, 1-33.
618 Geiger, R. (1927) *Das Klima der bodennahen Luftschicht. Ein Lehrbuch der Mikroklimatologie.*
619 Vieweg, Braunschweig.
620 Guisan, A. & Thuiller, W. (2005) Predicting species distribution: offering more than simple
621 habitat models. *Ecology Letters,* 8, 993-1009.
622 Hay, J.E. (1979) Calculation of monthly mean solar radiation for horizontal and inclined
623 surfaces. *Solar Energy,* 23, 301-307.
624 Hay, J.E. & McKay, D.C. (1985) Estimating solar irradiance on inclined surfaces: a review and
625 assessment of methodologies. *International Journal of Solar Energy,* 3, 203-240.
626 Hess, S.L. (1959) *Introduction to Theoretical Meteorology*. Holt, New York.
627 Hijmans, R.J., Cameron, S.E., Parra, J.L., Jones, P.G. & Jarvis, A. (2005) Very high resolution
628 interpolated climate surfaces for global land areas. *International Journal of*
629 *Climatology,* 25, 1965-1978.
630 Hunt, J., Kelliher, F., McSeveny, T. & Byers, J. (2002) Evaporation and carbon dioxide
631 exchange between the atmosphere and a tussock grassland during a summer drought.
632 *Agricultural and Forest Meteorology,* 111, 65-82.
633 Kalnay, E., Kanamitsu, R., Kistler, R., Collins, W., Deaven, D., Gandin, L., Iredell, M., Saha,
634 S., White, G., Woollen, J. et al. (1996) The NCEP/NCAR 40-year reanalysis project.
635 *Bulletin of the American Meteorological Society,* 77, 437-471.
636 Kearney, M.R. & Porter, W.P. (2017) NicheMapR – an R package for biophysical modelling:
637 the microclimate model. *Ecography*, 40, 664-674.
638 Kearney, M.R., Shamakhy, A., Tingley, R., Karoly, D.J., Hoffmann, A.A., Briggs, P.R. & Porter,
639 W.P. (2014) Microclimate modelling at macro scales: a test of a general microclimate

model integrated with gridded continental-scale soil and weather data. *Methods in Ecology and Evolution* 5, 273–286

Klok, E.J. & Oerlemans, J. (2002) Model study of the spatial distribution of the energy and mass balance of Morteratschgletscher, Switzerland. *Journal of Glaciology,* 48, 505-518.

Konzelmann, T., van de Wal, R.S., Greuell, W., Bintanja, R., Henneken, E.A. & Abe-Ouchi, A. (1994) Parameterization of global and longwave incoming radiation for the Greenland Ice Sheet. *Global and Planetary Change,* 9, 143-164.

Maclean, I.M.D, Hopkins, J.J., Bennie, J., Lawson, C.R. & Wilson, R.J. (2015) Microclimates buffer the responses of plant communities to climate change. *Global Ecology and Biogeography,* 24, 1340-1350.

Maclean, I.M.D., Suggitt, A.J., Wilson, R.J., Duffy, J.P. & Bennie, J. (2017) Fine-scale climate change: modelling spatial variation in biologically meaningful rates of warming. *Global Change Biology,* 23, 256-268.

Milling, C.R., Rachlow, J.L., Olsoy, P.J., Chappell, M.A., Johnson, T.R., Forbey, J.S., Shipley, L.A. & Thornton, D.H. (in press). Habitat structure modifies microclimate: An approach for mapping fine-scale thermal refuge. *Methods in Ecology and Evolution*.

Murphy, J. (2000) Predictions of climate change over Europe using statistical and dynamical downscaling techniques. *International Journal of Climatology*, 20, 489-501.

Pike, G., Pepin, N. & Schaefer, M. (2013) High latitude local scale temperature complexity: the example of Kevo Valley, Finnish Lapland. *International Journal of Climatology,* 33, 2050-2067.

Posselt, R., Mueller, R., Stöckli, R. & Trentmann, J. (2012) Remote sensing of solar surface radiation for climate monitoring—the CM-SAF retrieval in international comparison. *Remote Sensing of Environment,* 118, 186-198.

Potter, K.A., Woods, H.A. & Pincebourde, S. (2013) Microclimatic challenges in global change biology. *Global Change Biology,* 19, 2932-2939.

667 R Development Core Team (2017) *R: A Language and Environment for Statistical Computing,*
668 *R Foundation for Statistical Computing*. Vienna.
669 Rayner, N., Horton, E., Parker, D., Folland, C. & Hackett, R. (1996) Version 2.2 of the global
670 sea-ice and sea surface temperature data set, 1903–1994. *Climate Research*
671 *Technical Note 74*. Met Office, Exeter.
672 Robinson, E., Blyth, E., Clark, D., Comyn-Platt, E., Finch, J. & Rudd, A. (2015) *Climate*
673 *hydrology and ecology research support system meteorology dataset for Great Britain*
674 *(1961-2015) [CHESS-met] v1.2*. NERC Environmental Information Data Centre.
675 Ryan, B.C. (1977) A mathematical model for diagnosis and prediction of surface winds in
676 mountainous terrain. *Journal of Applied Meteorology,* 16, 571-584.
677 Suggitt, A.J., Platts, P.J., Barata, I.M., Bennie, J., Burgess, M.D., Bystriakova, N., Duffield, S.,
678 Ewing, S.R., Gillingham, P.K., Harper, A.B. et al. (2017) Conducting robust ecological
679 analyses with climate data. *Oikos*, 126, 1533-1541.
680 Suggitt, A.J., Wilson, R.J., Isaac, N.J.B., Beale, C.M., Auffret, A.G., August, T., Bennie, J.,
681 Crick, H.Q.P., Duffield, S., Fox, R.J. et al. (in press) Extinction risk from climate change
682 is reduced by microclimatic buffering. *Nature Climate Change*.
683 Wagner, W., Hollaus, M., Briese, C. & Ducic, V. (2008) 3D vegetation mapping using small-
684 footprint full-waveform airborne laser scanners. *International Journal of Remote*
685 *Sensing,* 29, 1433-1452.
686 Weller, G. & Holmgren, B. (1974) The microclimates of the arctic tundra. *Journal of Applied*
687 *Meteorology,* 13, 854-862.
688 Zhao, W. & Qualls, R.J. (2006) Modeling of long-wave and net radiation energy distribution
689 within a homogeneous plant canopy via multiple scattering processes. *Water*
690 *Resources Research,* 42, W08436.
691

692 **Supporting information**

693 Appendix S1. List and definitions of model parameters

694 Appendix S2. Supplementary methods

Appendix S3. Microclima package vignette

Appendix S4. Microclima function help files

Appendix S5. Microclima data requirements and sources

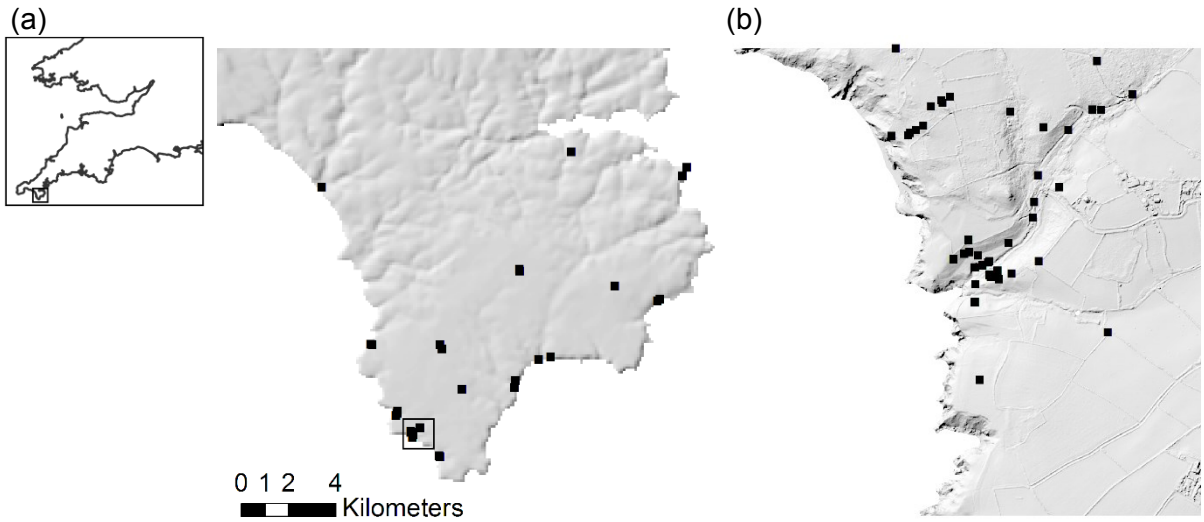

Fig. 1. Study areas depicting the locations covered by the mesoclimate (a) and microclimate (b) models. Black squares indicate the locations of iButton temperature data loggers deployed across the Lizard Peninsula between March 2010 and December 2010 (a) and at Caerthillean Cove in May 2010 (b). The shaded relief maps were derived from a DTM obtained the Tellus South West Project.

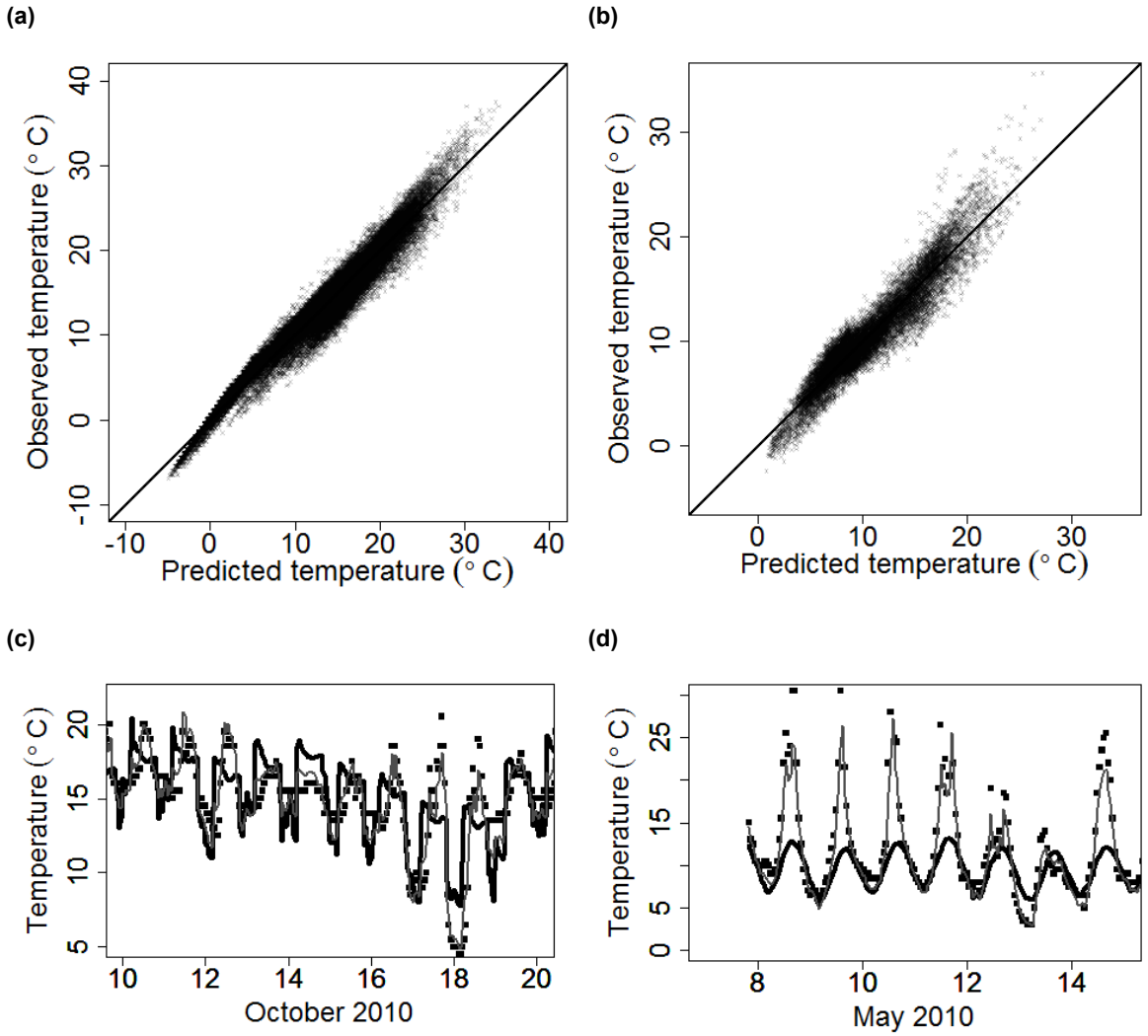

Fig. 2. Observed and predicted temperatures. In (a) temperatures recorded by iButtons place one metre above the ground are compared to outputs obtained from the mesoclimate model, and in (b) temperatures recorded by iButtons five cm above ground level are compared to the outputs of the microclimate model. In (c) recorded (black squares), modelled (grey line) and reference (black line) mesoclimate temperatures on a south-facing slope in Kynance Valley (49.979 ºN, 5.228 ºW) during October 2010 are shown. In (d) recorded (black squares), modelled (grey line) and reference (black line) microclimate temperatures on a south-facing slope in Caerthillean Valley (49.969 ºN, 5.215 ºW) during May 2010 are shown.

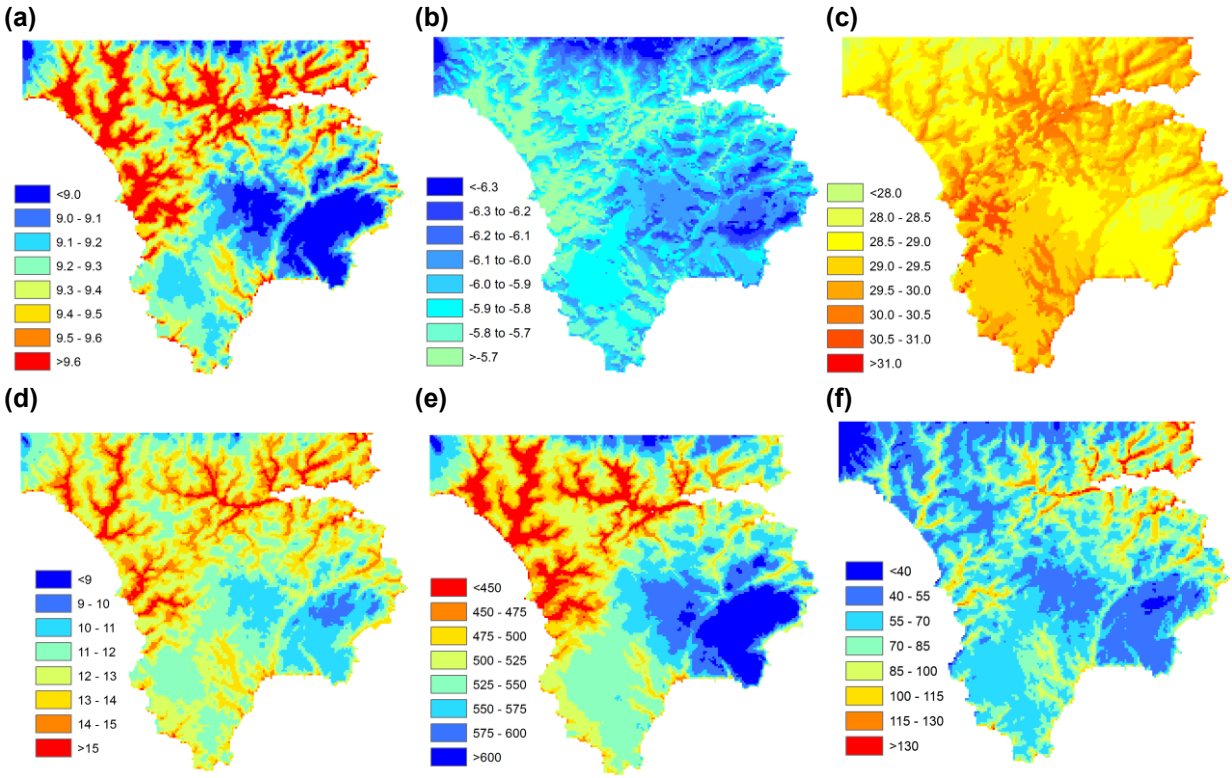

Fig. 3. Spatial variation in mesoclimate in 2010. (a) mean temperature (ºC); (b) minimum temperature (ºC); (c) maximum temperature (ºC); (d) accumulated degree-hours (thousands, base 10 ºC, ceiling 30 ºC); (e) hours of exposure to frost (<0 ºC); (f) hours of exposure to temperatures in excess of 25 ºC.

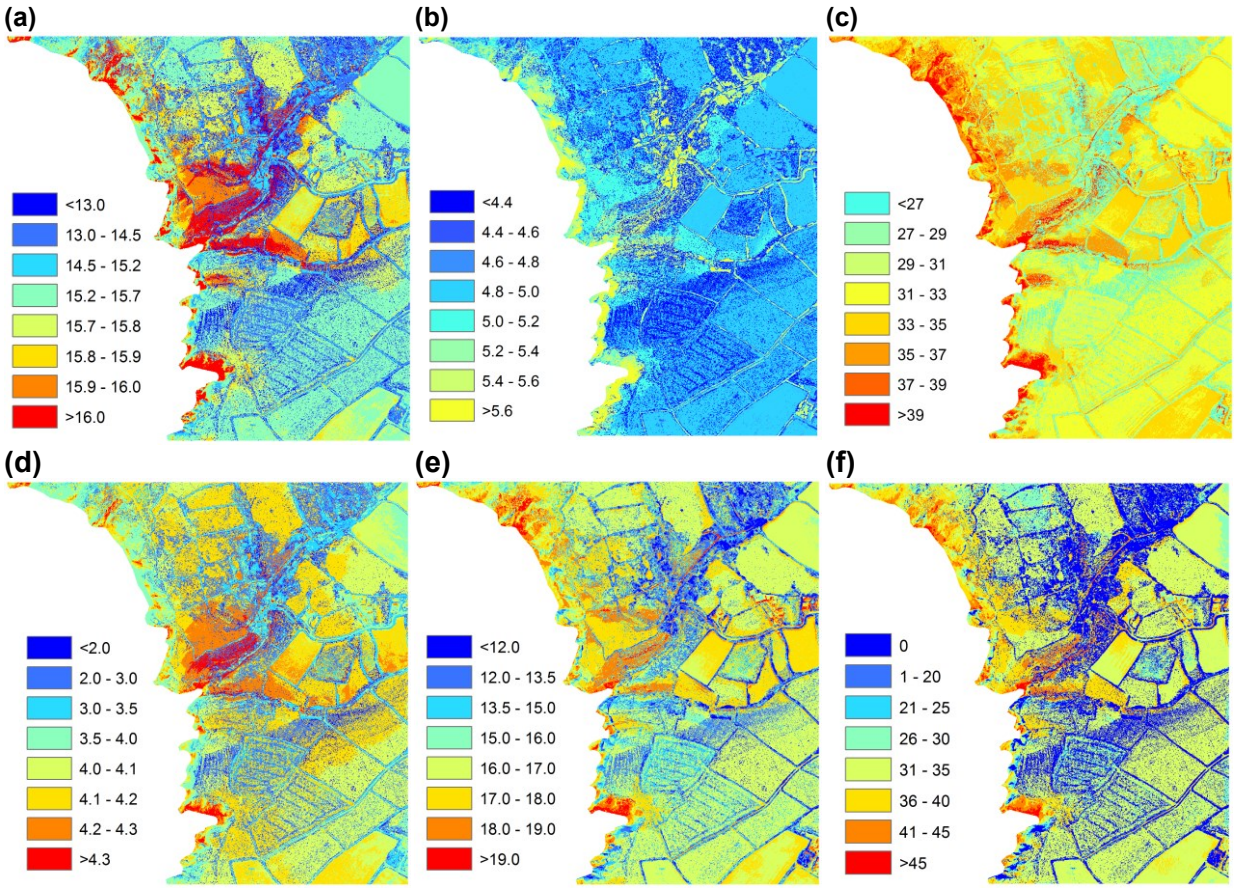

Fig. 4. Spatial variation in microclimate in May 2010. (a) mean temperature (ºC); (b) minimum temperature (ºC); (c) maximum temperature (ºC); (d) accumulated degree-hours (thousands, base 10ºC, ceiling 30ºC); (e) mean daily temperature range (ºC); (f) hours of exposure to temperatures in excess of 30 ºC.

Table 1. Summary of modelling approaches used for microclimate research.

	Regional climate models	**Land surface schemes (eg. JULES)**	**NicheMapR**	**Empirical DTM-based models**
Resolution	> five km	Point	Point	Usually >=1m
Vertical and/or horizontal fluxes considered	Both	Vertical	Vertical	None
Meso-scale processes represented	Yes	No	No	Yes
Computing requirements	High	Intermediate	Intermediate	Low
Physical basis	High	High	High	Low
Ecological relevance	Low	Intermediate	High	Intermediate

Table 2. Median, mean (± one standard deviation) model coefficients associated with meso- and microclimate model.

Variable	**Mesoclimate model**	**Microclimate model**
Intercept	0.210, 0.209 (0.05)	-0.989, -0.981 (0.105)
Radiation (MJ m^{-2} hr^{-1})	2.53, 2.260 (0.09)	4.28, 4.31 (0.313)
Wind factor (>3.66 meso; >0.398 micro)	0.447, 0.448 (0.101)	0.639, 0.638 (0.104)
Radiation x wind	-1.25, -1.21 (0.254)	-1.99, -2.02 (0.327)